ADVANCED MATERIALS
www.advmat.de

A Direct Evidence of Morphological Degradation on a Nanometer Scale in Polymer Solar Cells

*Christoph J. Schaffer, Claudia M. Palumbiny, Martin A. Niedermeier, Christian Jendrzejewski, Gonzalo Santoro, Stephan V. Roth, and Peter Müller-Buschbaum**

High power-conversion efficiencies that exceed 8.6%[1] and the ease of production even on flexible substrates promote polymer solar cells (PSC) to a revolutionary green technology. Nevertheless, shorter lifetimes, as compared to related inorganic technologies, hinder a commercial breakthrough. Thus, PSC stability emerged as a topic of increasing interest, and numerous pathways of ageing and degradation have been proposed.[2–4] Amongst them are alterations of the inner film morphology of the photo active layer,[5,6] which is crucial for the functioning of bulk-heterojunction[7] solar cells.[8–10] Whereas some extrinsic degradation mechanisms in polymer solar cells, such as photo-oxidation of the photo active layer[11] or corrosion and delamination of electrical contacts,[12–14] can be, to some extent, surpassed by suitable production steps, some intrinsic ones cannot be avoided so easily. Amongst them is the nanomorphological degradation of the photo active layer, which is evidenced by this work. Changes on the nanomorphology strongly influence the photovoltaic characteristics of polymer solar cells because the morphology plays a key role in how light is converted into electrical power. In high efficiency polymer solar cells, p- and n-type organic semiconductors are combined in the active layer, e.g., in polymer:fullerene systems, which are usually applied from solution. Thereby, phase separation gives rise to the formation of nanometer-scaled interpenetrating domains of a pure polymer, a pure fullerene, and a mixed phase.[15,16] Absorbed photons lead to the formation of excitons, which can be split into free extractable charge carriers at the interface between polymer and fullerene domains. However, this is possible only if the pathway to such an interface is shorter than the exciton diffusion length, ranging on a length scale of ten nanometers.[17,18] Otherwise, the exciton will recombine and consequently not contribute to current generation. If, due to morphological degradation, the mean distance between polymer-fullerene interfaces increases or the total interfacial area decreases, the solar cell current-output will diminish. The importance of the inner film morphology is also emphasized by the increment of the power conversion efficiency (PCE) when tuning the morphology by thermal annealing[19–21] or the use of solvent additives.[10,22] In this context it is clear that morphological transitions during operation act as a pathway of bulk-heterojunction solar cell degradation, as already proposed by different groups. It is known that thermal stress of some photovoltaic polymer:fullerene blends can induce the formation of micrometer-sized clusters of phenyl-C_{61}-butyric acid methyl ester (PCBM), as probed by transmission electron microscopy.[5] A decaying performance of the referred solar cells was attributed to the formation of these clusters and the resulting loss of interfacial area. Conings et al.[6] even proposed an empirical modified Arrhenius-like law which characterizes the decaying short-circuit current and allows for Oswald ripening of PCBM clusters. However, direct correlation of morphological transitions with a decaying device performance during operation is still missing and thus addressed in this work.

In this communication, we show an in situ investigation on a degrading model polymer solar cell where the evolution of both the nanomorphology of the active poly(3-hexylthiophen-2,5-diyl):phenyl-C_{61}-butyric acid methyl ester (P3HT:PCBM) layer and the current–voltage (*IV*) characteristics of the solar cell are simultaneously probed during operation. Further, we present a model which provides a direct correlation of the observed nanomorphological transitions and the decaying short-circuit current. In order to probe the active layer's nanomorphology, we use micro-focused grazing incidence small angle X-ray scattering (μGISAXS). In general, GISAXS is a technique allowing for the investigation of the bulk morphology of thin films on a scale ranging from several up to some hundreds of nanometers.[23] For μGISAXS, the X-ray beam is focused on a micrometer scale. Using this method, we demonstrate that operating the solar cell leads not only to degradation of the cell's performance but also to a significant alteration of its active layer morphology on a scale of a few tens of nanometers. Assuming a simple geometric model based on the findings of the μGISAXS measurements, we have been able to infer that the morphological transitions can fully explain the observed degradation of the solar cell's short-circuit current in an early stage of operation.

For investigating the active layer bulk morphology evolution, a polymer solar cell with an indium-doped tin oxide/poly(3,4-ethylenedioxythiophene): poly(styrenesulfonate)/P3HT:PCBM/aluminum (ITO/PEDOT:PSS/P3HT:PCBM/Al) architecture was installed in a self-made measurement chamber (Figure S1), which was evacuated for minimizing degradation due to oxygen. The initial morphology was probed with μGISAXS before illuminating the solar cell with simulated, air-mass 1.5 global

C. J. Schaffer, C. M. Palumbiny, M. A. Niedermeier, C. Jendrzejewski, Prof. P. Müller-Buschbaum
Technische Universität München
Physik-Department
Lehrstuhl für Funktionelle Materialien
James-Franck-Str., 1, 85748, Garching, Germany
E-mail: muellerb@ph.tum.de
Dr. G. Santoro, Dr. S. V. Roth
Deutsches Elektronen-Synchrotron DESY
Notkestr. 85, 22607, Hamburg, Germany

DOI: 10.1002/adma.201302854

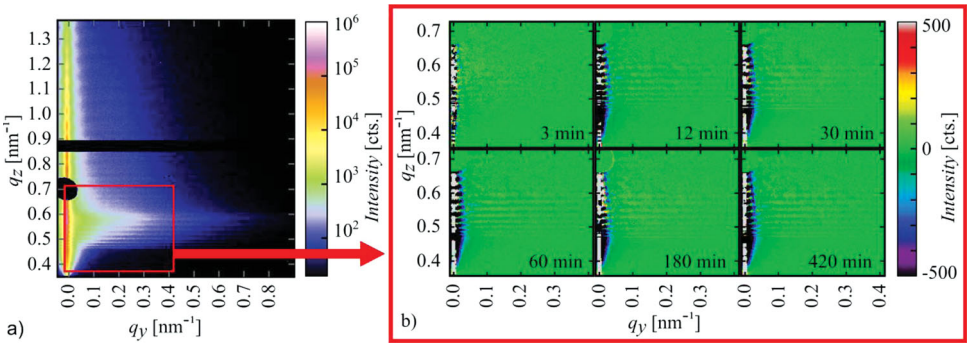

Figure 1. 2d μGISAXS patterns at different times. a) Initial 2d μGISAXS data of the polymer solar cell before illumination and *IV* measurements were started. b) The images show the difference signal of the 2d μGISAXS measurements obtained after different times of operation and the initial one within the marked window (red box). Negative values mean a loss of signal with respect to the initial measurement. All scattering data are corrected for beam flux variations.

(AM1.5G) sunlight. During illumination, current–voltage (*IV*) sweeps were recorded each 16 seconds (Figure S5). Further μGISAXS images were taken after 3, 12, 30, 60, 120, 180, 240, 300, 360, and 420 minutes. All μGISAXS data were corrected for X-ray flux variations. Further comments on μGISAXS data acquisition and analysis can be found in Section S3 of the supporting information. In order to highlight the changes that took place during solar cell operation, the initial μGISAXS pattern, shown in **Figure 1**a, was subtracted from the later ones. It can be seen from these difference images depicted in Figure 1b, that the lateral scattering signal decreased in a range of lateral X-ray momentum transfer $q_y = 10^{-2}$ nm^{-1} to 10^{-1} nm^{-1}, corresponding to structures on a length scale ranging from 60 to 600 nm. At the same time, the intensity increased at very low q_y values corresponding to larger structures. This trend holds particularly in the so-called Yoneda region,[24] where the lateral scattering is strongest (red box in Figure 1a). The lateral variations in the μGISAXS data propose that medium-sized structures fade away in favour of larger ones and indicate that the film morphology changed during operation of the solar cell. Further investigation of the morphology changes was performed by extracting and modeling horizontal line cuts from the normalized 2d μGISAXS data at the material-specific Yoneda peak[24] of P3HT, where the strongest scattering contribution of P3HT occur. These cuts give information about lateral structures formed by P3HT or its voids (PCBM) inside the active layer. Modeling the data revealed the presence of three distinct substructures, each being characterized by mean object radii $<R_i>$ and distances $<d_i>$ on distinct length scales. The time evolution of the feature sizes $<R_i>$ and inter-distances $<d_i>$ is shown in **Figure 2**. As expected from the differential μGISAXS data, the morphology shows significant transitions with operating time in a range of 10^{-2} nm^{-1}

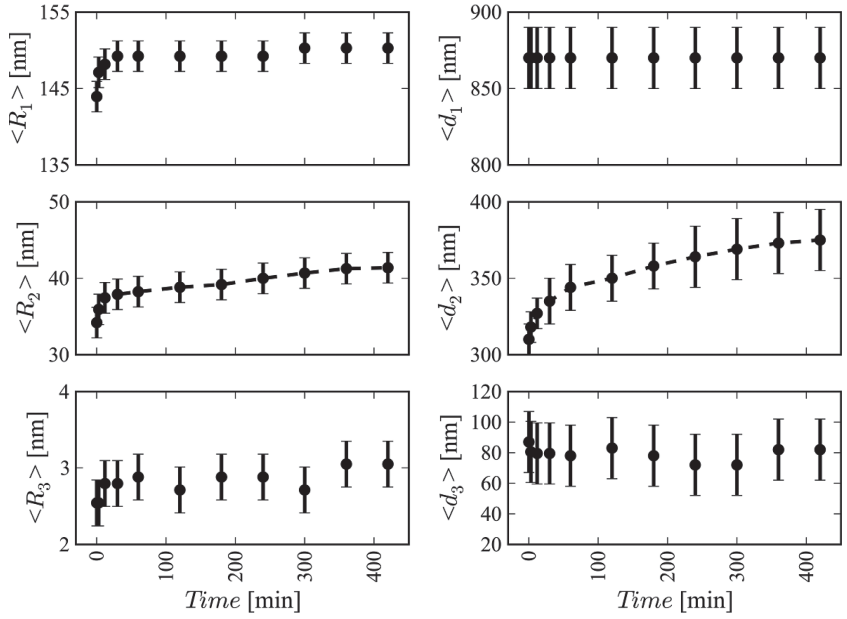

Figure 2. Time evolution of the substructure parameters as obtained from modeling the horizontal line cuts of the 2d μGISAXS data. The dashed lines are a guide to the eye.

Adv. Mater. **2013**,
DOI: 10.1002/adma.201302854

to 10^{-1} nm^{-1}. These q_y-values correspond to the mean radii and distances $<R_2>$ and $<d_2>$, respectively. For $q_y < 10^{-2}$ nm^{-1} and $q_y > 10^{-1}$ nm^{-1}, the modeled data correspond to mean radii $<R_1>$ around 140 nm and $<R_3>$ between 2.5 and 3 nm with site-to-site distances $<d_1>$ around 870 nm and $<d_3>$ around 70 nm. Both, these substructures, 1 and 3, have been reported and attributed to PCBM aggregates by Ruderer et al.[15] In general, we find that all objects grow with time. However, only the intermediate substructure ($<R_2>$, $<d_2>$) is expected to strongly influence the solar cell performance since the length scales of both $<R_1>$ and $<R_3>$ do not match the exciton diffusion length at any time. Therefore, the observed loss of short-circuit current can only be attributed to changes in the intermediate-sized domains. This is also in good agreement with earlier research proposing ideal inter distances of a few hundreds of nm.[9,25] Furthermore, a significant growth of large PCBM clusters did not occur due to the limited operation temperature of below 45 °C (Figure S3), as confirmed by ex post optical and atomic force microscopy (AFM) measurements (Figures S6, S7). For the intermediate domains, not only the mean object radius increased from around 34 nm to over 40 nm during illumination but also the mean distance between such objects increased from around 310 nm to roughly 370 nm. This implies that small domains vanished in favour of larger ones during solar cell operation. Thus, the intermediate domains grew with time while effectively drifting apart from each other. The presented morphological evolution can explain the observed decay of the short-circuit current. Basing on morphological information extracted from modeling the μGISAXS data, we assumed a geometrical model, consisting of cylinders of one active material in a mixed P3HT:PCBM matrix, for predicting the short-circuit current density. Without loss of generality, these cylinders are assumed to consist of P3HT. The following assumptions were also considered.

(a) The P3HT domains (represented by red circles in **Figure 3**) are surrounded by a ring with a constant thickness l, which is referred to as an effective harvesting length (green rings in Figure 3). Holes that are created within this ring can reach the P3HT core and efficiently be extracted. The average cross-sectional cumulated area of one illuminated cylinder and its corresponding ring (red and green respectively) is referred to as the mean active area $A_A = \pi \left\langle (R_2 + l)^2 \right\rangle$. In order to explain the initially measured short-circuit current density, l is estimated to a lower limit of $l \geq 55$ nm (Section S4)
(b) Only intermediate domains ($<R_2>$, $< d_2>$) cause the charge carrier generation.
(c) Only photons absorbed within the active area can create charge carrier pairs which contribute to the photocurrent with an overall probability p.
(d) Since the experiment was carried out under vacuum conditions, degradation due to chemical alterations of the active compounds is neglected, i.e., the probability p of a photon absorbed within the active area to create a charge carrier is constant in time.

Taking these assumptions, an expression for the normalized short-circuit current density $J_{SC}^{norm}(t)$, which is governed by the time evolution of the active area, can be stated as in Equation (1).

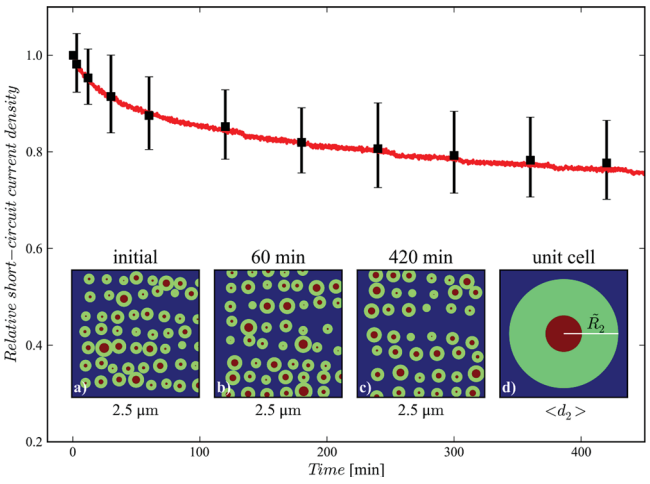

Figure 3. Simulated and measured short-circuit current. Black squares represent the relative short-circuit current as theoretically expected from the time-dependent morphology probed by μGISAXS. The red line indicates the measured normalized short-circuit current density. Error bars are estimated from the error in the structure parameters. a–c) Visualisation of the inner film morphology at the different times stated above as generated during the Monte-Carlo simulation. The images represent an excerpt of 2.5 μm × 2.5 μm. The red circles represent domains of pure material. The green cylinder walls represent, together with the red core, the active area of the solar cell where absorbed photons contribute to charge carrier generation. Photons absorbed in the blue phase do not contribute. d) Unit cell of a square lattice as assumed for predicting the theoretical values of the normalized short-circuit current density. The unit cell side length is $<d_2>$, $R_2 = \sqrt{\langle (R_2 + l)^2 \rangle}$ defines the radius of an averaged active domain.

$$J_{SC}^{norm}(t) = \frac{J_{SC}(t)}{J_{SC}(0)} = \frac{p \cdot Q \cdot I \cdot A_A(t) \cdot A_T(0)}{p \cdot Q \cdot I \cdot A_A(0) \cdot A_T(t)} = \frac{\left\langle \left(R_2(t) + l\right)^2 \right\rangle \cdot \left\langle d_2(0) \right\rangle^2}{\left\langle \left(R_2(0) + l\right)^2 \right\rangle \cdot \left\langle d_2(0) \right\rangle^2} \quad (1)$$

In this expression, $J_{SC}(t)$ is the (absolute) short-circuit current density at a time t, I is the illumination intensity, Q is the elementary charge, p is the probability for generating extractable charge carriers, A_T is the mean total area per object, and A_A is the mean active area. A_T is approximated by the area of a quadratic unit cell with a side length of $<d_2>$. Such a cell is depicted in Figure 3d, where $R_2 = \sqrt{\langle (R_2 + l)^2 \rangle}$ denotes the (Gaussian) mean radius of an active domain. From Equation (1), we deduce the expected normalized short-circuit current $J_{SC}^{norm}(t)$ directly from the μGISAXS model parameters at each time by applying the morphological information from μGISAXS. The theoretically expected normalized short-circuit current density (black squares) at each μGISAXS measurement time is shown, together with the measured one (red solid line), in Figure 3. An effective harvesting length of $l = 80$ nm has been chosen, which leads to a good match of the calculated and the measured short-circuit current densities while allowing for $p < 1$.

The modeling of the μGISAXS data was performed assuming a 1-dimensional paracrystalline lattice. Therefore, a Monte Carlo simulation based on such a structure has been performed. The simulation confirms the results found above

(Figure S13). The inlets in Figure 3a-c show exemplary image sections of the simulated morphologies after 0, 1 and 7 hours of solar cell operation. Although the active domains expand with time, their occurrence fades sufficiently fast and the ratio of active and total area consequently decreases over time, leading to a loss of solar cell current output. Based on the excellent agreement of theoretical and measured data, we conclude that the loss of short-circuit current density was mainly driven by the evolving nanomorphology of the photo active layer.

Concluding, we propose a model of morphological degradation, where active layer domains, which are suitable for efficiently harvesting light, drift apart from each other in the sense that smaller domains vanish whereas larger ones grow. This is confirmed by in situ µGISAXS measurements. This drift causes a reduction of the overall area of a polymer solar cell's photo active layer in which light is converted into electrical power. Consequently, the output current of the solar cell decreases. This model is capable of fully explaining the loss of the short-circuit current observed during operation of the investigated system. In this way, the decaying short-circuit current is, for the first time, directly and quantitatively correlated with the morphological changes of the photoactive layer as a result of organic solar cell degradation. This provides a direct evidence of morphological degradation in a polymer solar cell. Considering a relative loss of nearly 25% in the short-circuit current density for the investigated model solar cell within 7 operating hours, the observed changes in the nanomorphology appear as an extremely important pathway of degradation in polymer solar cells, which needs to be fully considered when designing and fabricating polymer solar cells. Moreover, the present work can contribute to better tailoring polymer solar cells' stability since it seems feasible to tune the initial morphology such that, during the early stages of operation, the active layer evolves to a state with an optimal morphology for solar energy conversion.

Experimental Section

Polymer solar cells were prepared by spin coating a solution of P3HT:PCBM (1:1, total concentration: 24 mg mL^{-1} in chlorobenzene) on top of a PEDOT:PSS-coated ITO substrate (Solems). The ITO-substrates were cleaned with different solvents (Alconox solution, ethanol, acetone and 2-propanol) and by oxygen plasma before being coated with PEDOT:PSS (Sigma-Aldrich). Poly(3-hexylthiophene-diyl) (P3HT) and [6,6]-phenyl-C_{61}-butyric acid methyl ester (PCBM) were purchased from ONE-Material and NanoC respectively and used as received. After spin coating the active layer, aluminum contacts were deposited by physical vapour deposition (PVD) at a pressure of 2×10^{-5} mbar. Afterwards, the solar cells were thermally annealed for 10 minutes at 140 °C in an argon-filled glove box, where they were subsequently sealed in KF flange steel containers for the transport to the synchrotron facility. The samples were stored in this way for five days and encountered air contact for less than 10 minutes only while being transferred from the transport container into the measurement chamber. In situ µGISAXS measurements were performed at the P03/MiNaXS beamline of the PETRA III storage ring at DESY (Hamburg, Germany),[26] using a micro focused X-ray beam with a beam size of 28 µm × 23 µm (horizontal × vertical) and a wavelength of 0.1086 nm. A sample-detector distance of 3698 mm and an incident angle of 0.35° were employed.

For the µGISAXS measurements, an evacuated chamber (2×10^{-1} mbar) with Kapton windows for X-rays and a quartz window (for illumination of the solar cell) was used. The chamber has been designed and built in such a way that the *IV* characteristic curves of the solar cell and the µGISAXS patterns can be recorded simultaneously. The scattering data were acquired at three different positions within a distance of less than 1 mm to the Al electrode. The exposure time was 2 s in order to minimize radiation damage (Section S3) and µGISAXS data were acquired before the illumination started and then after 3, 12, 30, 60, 120, 180, 240, 300, 360, and 420 minutes. *IV* curves were recorded constantly each 16 seconds using a Keithley SourceMeter 2400 series during the full time of illumination. Illumination was performed using a 150 W Xenon short arc lamp (Perkin Elmer PX5) employing an intensity of 100 mW/cm^2. The lamp intensity increased less than 3% during continuous operation for more than 8 h.

Supporting Information

Supporting Information is available from the Wiley Online Library or from the author.

Acknowledgements

C.J.S. thanks the Bavarian State Ministry of Sciences, Research and Arts for funding this work via the International Graduate School "Materials Science of Complex Interfaces" (CompInt) and Dr. Matthias A. Ruderer for discussion and preliminary work. C.M.P. acknowledges financial support by the "International Graduate School of Science and Engineering" (IGSSE) and M.A.N. by TUM Solar in the frame of the Bavarian Collaborative Research Project "Solar Technologies Go Hybrid" (SolTec).

Received: June 23, 2013
Published online:

[1] L. Dou, J. You, J. Yang, C.-C. Chen, Y. He, S. Murase, T. Moriarty, K. Emery, G. Li, Y. Yang, *Nat. Photonics* **2012**, *6*, 180.
[2] M. Jørgensen, K. Norrman, S. A. Gevorgyan, T. Tromholt, B. Andreasen, F. C. Krebs, *Adv. Mater.* **2012**, *24*, 580.
[3] M. Jørgensen, K. Norrman, F. C. Krebs, *Sol. Energy Mater. Sol. Cells* **2008**, *92*, 686.
[4] N. Grossiord, J. M. Kroon, R. Andriessen, P. W. M. Blom, *Org. Electron.* **2012**, *13*, 432.
[5] S. Bertho, G. Janssen, T. J. Cleij, B. Conings, W. Moons, A. Gadisa, J. D'Haen, E. Goovaerts, L. Lutsen, J. Manca, D. Vanderzande, *Sol. Energy Mater. Sol. Cells* **2008**, *92*, 753.
[6] B. Conings, S. Bertho, K. Vandewal, A. Senes, J. D'Haen, J. Manca, R. A. J. Janssen, *Appl. Phys. Lett.* **2010**, *96*, 163301.
[7] G. Dennler, M. C. Scharber, C. J. Brabec, *Adv. Mater.* **2009**, *21*, 1323.
[8] H. Hoppe, M. Niggemann, C. Winder, J. Kraut, R. Hiesgen, A. Hinsch, D. Meissner, N. S. Sariciftci, *Adv. Funct. Mater.* **2004**, *14*, 1005.
[9] M. A. Ruderer, S. Guo, R. Meier, H. Y. Chiang, V. Körstgens, J. Wiedersich, J. Perlich, S. V. Roth, P. Müller-Buschbaum, *Adv. Funct. Mater.* **2011**, *21*, 3382.
[10] J. Peet, J. Kim, N. E. Coates, W. L. Ma, D. Moses, A. J. Heeger, G. C. Bazan, *Nat. Mater.* **2007**, *6*, 497.
[11] T. Tromholt, M. Manceau, M. Helgesen, J. E. Carlé, F. C. Krebs, *Sol. Energy Mater. Sol. Cells* **2011**, *95*, 1308.
[12] J. McElvain, H. Antoniadis, M. Hueschen, J. Miller, D. Roitman, J. Sheats, R. Moon, *J. Appl. Phys.* **1996**, *80*, 6002.
[13] M. Schaer, F. Nüesch, D. Berner, W. Leo, L. Zuppiroli, *Adv. Funct. Mater.* **2001**, *11*, 116.
[14] J. S. Kim, P. K. Ho, C. E. Murphy, N. Baynes, R. H. Friend, *Adv. Mater.* **2002**, *14*, 206.

[15] M. A. Ruderer, R. Meier, L. Porcar, R. Cubitt, P. Müller-Buschbaum, *J. Phys. Chem. Lett.* **2012**, *3*, 683.
[16] B. A. Collins, J. R. Tumbleston, H. Ade, *J. Phys. Chem. Lett.* **2011**, *2*, 3135.
[17] D. E. Markov, E. Amsterdam, P. W. M. Blom, A. B. Sieval, J. C. Hummelen, *J. Phys. Chem. A* **2005**, *109*, 5266.
[18] P. E. Shaw, A. Ruseckas, I. D. W. Samuel, *Adv. Mater.* **2008**, *20*, 3516.
[19] D. Chirvase, J. Parisi, J. Hummelen, V. Dyakonov, *Nanotechnology* **2004**, *15*, 1317.
[20] J. Jo, S. S. Kim, S. I. Na, B. K. Yu, D. Y. Kim, *Adv. Funct. Mater.* **2009**, *19*, 866.
[21] Y. Kim, S. Cook, S. M. Tuladhar, S. A. Choulis, J. Nelson, J. R. Durrant, D. D. Bradley, M. Giles, I. McCulloch, C.-S. Ha, *Nat. Mater.* **2006**, *5*, 197.
[22] Y. Liang, Z. Xu, J. Xia, S. T. Tsai, Y. Wu, G. Li, C. Ray, L. Yu, *Adv. Mater.* **2010**, *22*, E135.
[23] P. Müller-Buschbaum, *Anal. Bioanal. Chem.* **2003**, *376*, 3.
[24] Y. Yoneda, *Phys. Rev.* **1963**, *131*, 2010.
[25] C. R. McNeill, A. Abrusci, I. Hwang, M. A. Ruderer, P. Müller-Buschbaum, N. C. Greenham, *Adv. Funct. Mater.* **2009**, *19*, 3103.
[26] A. Buffet, A. Rothkirch, R. Dohrmann, V. Korstgens, M. M. Abul Kashem, J. Perlich, G. Herzog, M. Schwartzkopf, R. Gehrke, P. Muller-Buschbaum, *J. Synch. Rad.* **2012**, *19*, 647.